

Multiple Gas Seepage Mechanisms and Production Development Research for Shale Gas Reservoirs from Experimental Techniques and Theoretical Models

Zhiming Hu, Xianggang Duan, Jin Chang, Xiaowei Zhang, Shangwen Zhou, Yingying Xu,* Rui Shen, Shusheng Gao, and Ying Mu



Cite This: *ACS Omega* 2023, 8, 3571–3585



Read Online

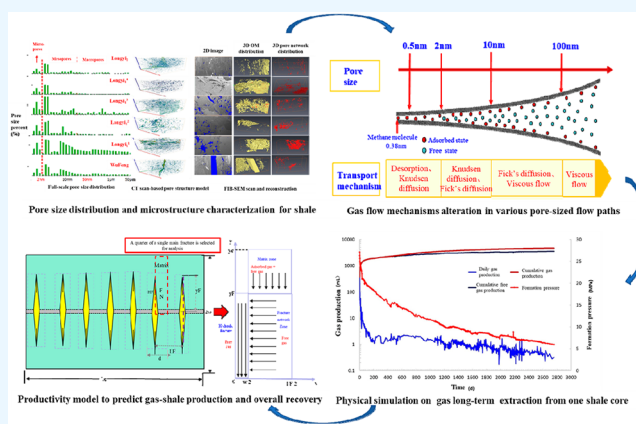
ACCESS |

Metrics & More

Article Recommendations

Supporting Information

ABSTRACT: Shale gas seepage theory provides a scientific basis for dynamically analyzing the physical gas flow processes involved in shale gas extraction and for estimating shale gas production. Conventional experimental techniques and theoretical methods applied in seepage research are unable to accurately illustrate shale gas mass transfer processes at the micro- and nanoscale. In view of these scientific issues, the knowledge of seepage mechanisms and production development design was improved from the perspective of experimental techniques and theoretical models in the paper. First, multiple techniques (e.g., focused ion beam scanning electron microscopy and a combination of mercury intrusion porosimetry and adsorption measurement techniques) were integrated to characterize the micro- and nanopore distribution in shales. Then, molecular dynamics simulations were carried out to analyze the microscale distribution of gas molecules in nanopores. In addition, an upscaled gas flow model for the shale matrix was developed based on molecular dynamics simulations. Finally, the coupled flow and productivity models were set up according to a long-term production physical simulation to identify the production patterns for adsorbed and free gas. The research results show that micropores (diameter: <2 nm) and mesopores (diameter: 2–50 nm) account for more than 70% of all the pores in shales and that they are the primary space hosting adsorbed gas. Molecular simulations reveal that microscale adsorption layers in organic matter nanopores can be as thick as 0.7 nm and that desorption and diffusion are the main mechanisms behind the migration of gas molecules. An apparent permeability model that comprehensively accounts for adsorption, diffusion, and seepage was developed to address the deficiency of Darcy's law in characterizing gas flowability in shale reservoirs. The productivity model results for a certain gas well show that the production in the first three years accounts for more than 50% of its estimated ultimate recovery and that adsorbed gas contributes more to the annual production than free gas in the eighth year. These research results provide theoretical and technical support for improving the theoretical understanding of shale gas seepage and optimizing shale gas extraction techniques in China.



INTRODUCTION

Through more than a decade of exploration and development efforts, China has made significant strides in shale gas development, through a combination of multiple maturing subjects including shale gas exploration and development as well as geological engineering. It is estimated that China's national shale gas production increased by 50% year over year in 2019, showing a strong momentum of growth.^{1,2} Shale gas seepage and development theories provide a theoretical basis for dynamically analyzing the gas flow process of gas shale systems, estimating shale gas productivity, and moreover effectively improving the overall gas recovery of a single well, which is substantially supportive to the upscaled shale gas production in southern Sichuan.^{3,4}

Highly heterogeneous shale reservoirs are abundant in micro- and nanopores as the primary space for gas accumulation and seepage. However, poor pore interconnectivity can lead to an extremely low gas flowability. Consequently, vertical wells are generally unable to extract gas out of tight gas shale without stimulated reservoir

Received: September 6, 2022
Accepted: December 15, 2022
Published: January 13, 2023



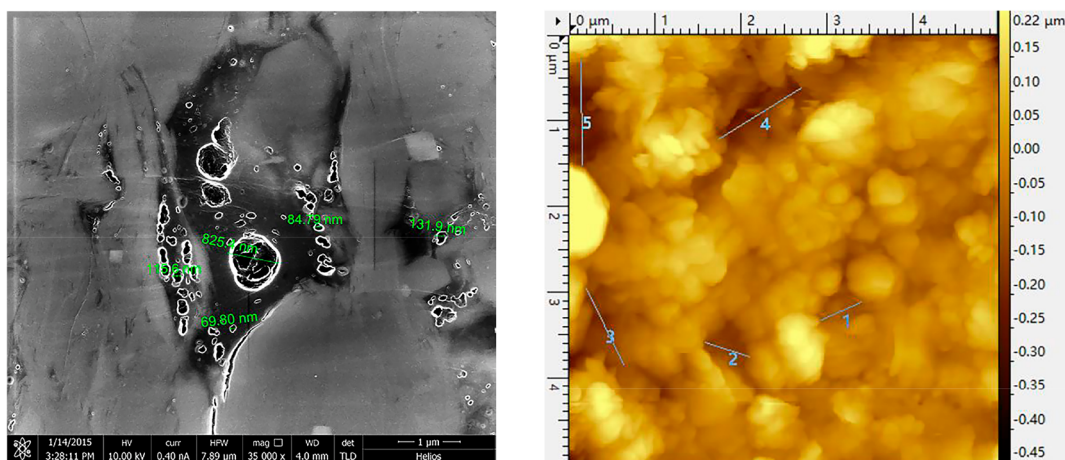


Figure 1. Comparison of FIB–SEM and AFM images of shale samples.

volume.^{5,6} With complex fracture networks stimulated through horizontal well approaches and volumetric fracturing techniques, several hundreds of thousands of or even over a million cubic meters of gas were produced out of shale each day during the trials, which lasted for several years.^{7,8} In addition, complicated shale gas flow mechanisms in shale formations result from the presence of micropores and the shale gas occurrence state. Therefore, the experimental techniques and theoretical methods applied in conventional oil/gas systems are limited in illustrating shale gas mass transport—a phenomenon that involves desorption, diffusion, and seepage.⁹ As a result, production decline analysis and productivity evaluation have been rather challenging so far.

During the incipient stage of its endeavor to utilize shale gas, systematical investigations into characterizing porous media and gas seepage patterns of shale systems were initially conducted in China, resulting in an inaccurate knowledge of the shale gas development pattern since then. The failure to focus on shale gas of marine facies in China and the absence of adequately targeted and instructive development techniques, to some extent, impeded increases in the gas extraction and overall recovery in shale reservoirs.^{10,11} Our research has been dedicated to addressing scientific problems such as the pore distribution characterization and gas flow mechanisms and development pattern identification for gas shale systems. First, a comprehensive reservoir microstructure characterization method was developed to evaluate micro- and nanopore occurrences in shale reservoirs from quantitative and qualitative perspectives. Subsequently, investigative techniques (e.g., molecular dynamics simulation and high-pressure flow-pattern evaluation) were established to examine shale gas accumulation and migration mechanisms at the micro- and nanoscale. Moreover, gas flowability evaluation and prediction were achieved through setting up a theoretically mathematical model. In the end, an indoor physical simulation was put forward to clarify shale gas extraction out of a shale matrix by simulating ultra-long-term production of shale cores, aimed at determining dynamic production decline patterns of gas shale systems. A multiscale coupled model was also established to provide a mathematical tool for production yield estimates and analyzing production declines.

■ MICROSTRUCTURAL CHARACTERIZATION TECHNIQUES FOR SHALE RESERVOIRS

Shale reservoirs have a more complex pore structure, as they are unconventional reservoirs integrated with source rocks. The level of development of micro- and nanopores affects gas accumulation and seepage in shale reservoirs. Determining the characteristics of the pore structure of a shale reservoir is vitally important for estimating its reserves and evaluating its development potential.¹² Pores in shale reservoirs range from several nanometers to several hundreds of microns in size. This wide range presents a challenge to the use of a single measurement method to fully characterize the pore size distribution and pore structure of shale reservoirs.¹³ Currently, the pore structure of shale reservoirs is primarily examined through imaging and quantitative tests.^{14–17} The main imaging methods include high-resolution focused ion beam scanning electron microscopy (FIB–SEM), transmission electron microscopy, atomic force microscopy (AFM), small-angle X-ray scattering, and nanocomputed tomography (CT).^{18–28} FIB–SEM, known for its high-resolution capabilities, can be used to image nanopores and is primarily employed in two-dimensional (2D) observations.^{23,24} High-resolution CT can be used for nondestructive scanning and three-dimensional (3D) reconstruction of nanopores in samples. However, CT scans over a wide field of view have low accuracy due to instrument limitations.²⁹ Some new techniques, such as small-angle neutron scattering (SANS) and ultra-SANS, use a neutron beam to penetrate a shale sample and obtain information on its pore structure through measurement of the intensity of radiation scattered within a specific range.²⁵ AFM can be used to image the 3D morphology of shale samples in their true state and display pore networks composed of micro- and nanopores connected through relatively small throats (Figure 1). This technique, however, has two deficiencies: a very small scan area and a low scan rate.^{26–28}

High-pressure mercury intrusion porosimetry (MIP), low-temperature nitrogen (N₂) adsorption, carbon dioxide (CO₂) adsorption, and nuclear magnetic resonance (NMR) are among the techniques commonly used to quantify pore-size distribution.^{15,29–32} MIP involves the injection of mercury into pores under a high pressure up to 350 MPa and has a 3.7 nm (pore radius) detection precision. However, the saturation of mercury injected into a shale sample is generally low, and the

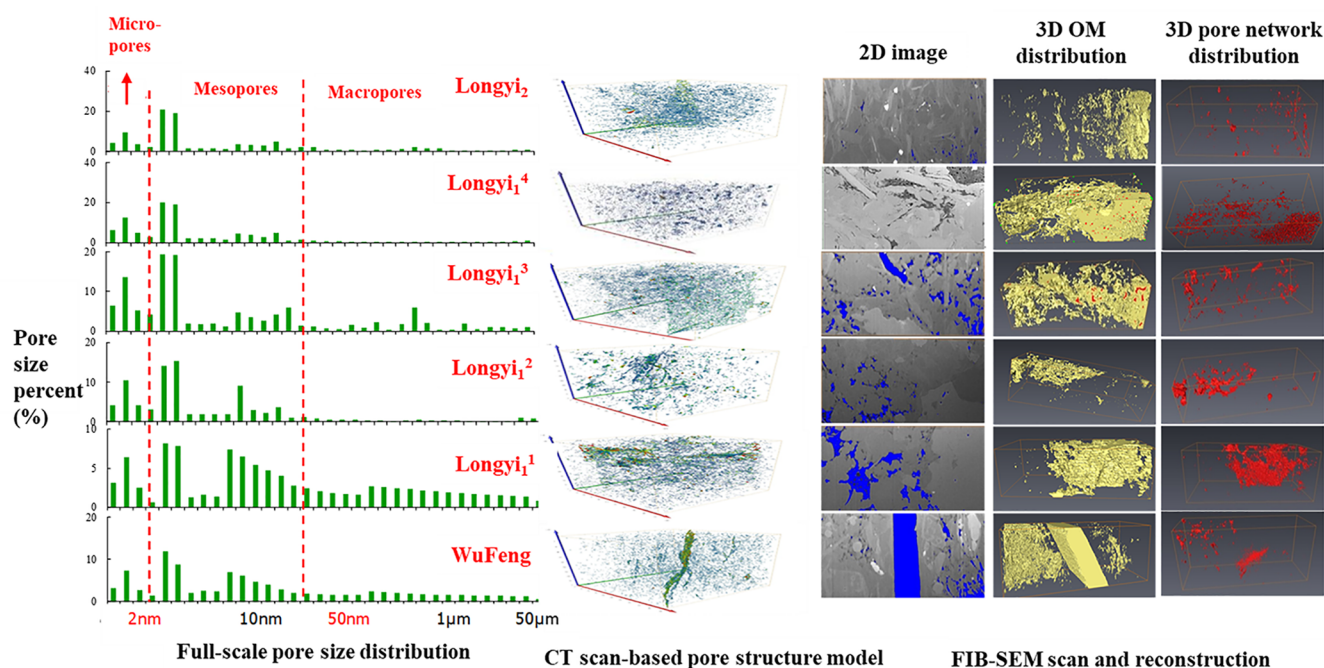


Figure 2. Full-range pore-size distribution, CT scanning, and FIB-SEM results for shale samples.

high pressure required for the process can deform and damage the pores.²⁸ According to the capillary condensation theory and the Barrett–Joyner–Halenda model, the effective pore-size range that can be derived from low-temperature nitrogen adsorption curves is 2–200 nm for shale samples.³⁰ The CO₂ adsorption technique can be used to measure micropores smaller than 2 nm and down to 0.35 nm in diameter.³³ NMR determines pore-size distribution based on the T₂ relaxation time of the saturated fluid in the pores. This technique is advantageous due to its general insusceptibility to the effects of the matrix component and its ability to produce relatively accurate porosity and pore-size distribution estimates for rock layers. Despite its advantages, NMR has limited capabilities in the characterization of multiscale pores in shale samples due to two factors: (1) saturating shale samples with a fluid is difficult due to the small pores and (2) the relationship between T₂ and the pore size generally relies on empirical evidence.^{34–36}

Use of multiple techniques in tandem is required to better characterize the multiscale pore structure of a shale sample and its pore-size distribution. Six core samples of the section extending from the Wufeng (WF) formation (Fm) to the Longmaxi (LMX) Fm, retrieved from well Z201 in western Chongqing, were subjected to parallel tests using methods such as FIB-SEM (minimum resolution: 0.9 nm), CT scanning (resolution: 300 nm), high-pressure MIP, low-temperature N₂ adsorption, and CO₂ adsorption. Full-range pore-size distribution curves were generated by combining the quantitative measurements obtained using the high-pressure MIP, low-temperature N₂ adsorption, and CO₂ adsorption techniques. Pores smaller than 2 nm, 2–50 nm, and larger than 50 nm in diameter were measured using the CO₂ adsorption, low-temperature N₂ adsorption, and high-pressure MIP techniques, respectively.^{15,31} Analysis of the full-range pore-size curves (Figure 2) reveals that the pores in the shale in this well primarily consist of mesopores (2–50 nm in diameter, 51.85–73.08% average: 63%) and, to a smaller extent, micropores (<2 nm in diameter, 11.9–25.3%, average: 15%).

Our observation of the 2D FIB-SEM scans and the reconstructed 3D distribution of the organic matter (OM) and pore network shows that the OM pores in the shale in the LMX Fm in western Chongqing are mostly circular, oval, or interfacial in shape on the plane and that their diameters vary widely, from nanometers to microns. Relatively well-developed pores are present in the Longyi₁³ and Longyi₁¹ sublayers of the LMX Fm and the WF Fm. The Longyi₁¹ sublayer and the WF Fm contain relatively well-developed throats and relatively large slit-shaped pores and have the highest proportion (>30%) of macropores. A large number of macropores lead to high pore connectivity and provide channels for gas diffusion and seepage. Therefore, the Longyi₁¹ sublayer and the WF Fm are the best-quality reservoirs with the most developed accumulation and seepage space in this region, and they are the current layers of interest for development.

■ MASS TRANSPORT MECHANISMS AND GAS FLOWABILITY EVALUATION MODEL

Microscopic Mass Transport Mechanisms. Shale gas exists and migrates primarily in nanopores. When the free path of motion of gas molecules approaches the size of the nanthroats, the microscale effects of gas mass transport manifest themselves, while the impact of several mechanisms (e.g., desorption, slip, and diffusion) on the gas transport process becomes more pronounced. These factors preclude the direct use of some theories and experimental techniques applicable to conventional gas reservoirs to investigate flow patterns in shale gas reservoirs.^{31,37,38} Therefore, more microscopic methods, such as the molecular dynamics and lattice Boltzmann methods (LBM) and pore network models, are employed to study shale gas and its mass transfer mechanisms at the microscale.^{39–48}

Pore network models can provide a relatively true reflection of the geometric topography and connectivity in core samples and are the most computationally efficient. However, the currently available models are rare for quantification of the

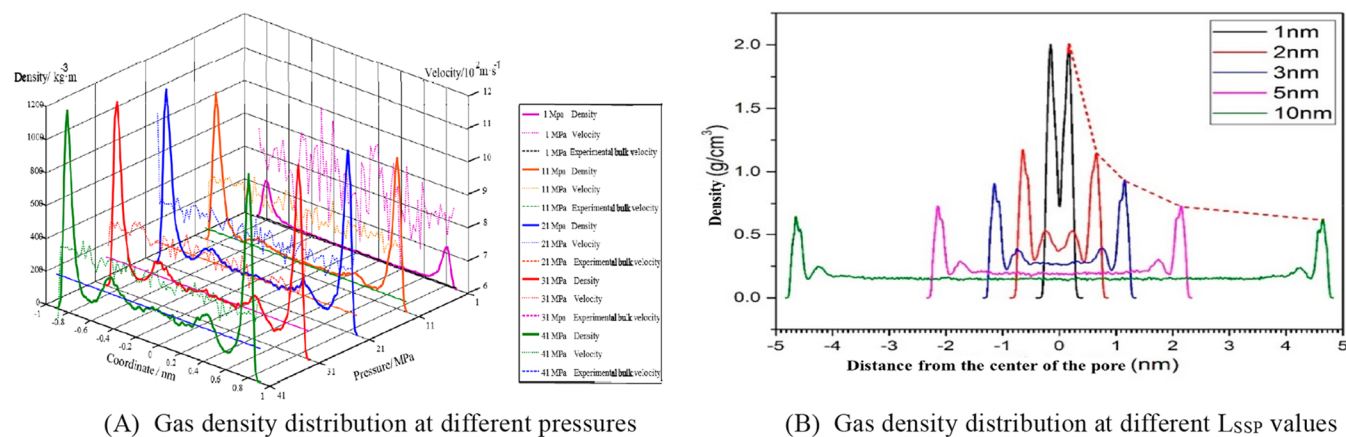


Figure 3. Density distribution curves of the gas.

irregularity of porous media for gas shale.^{39,40} The LBM can directly simulate fluid flow in a core sample after a simple binarization treatment of its SEM or CT image. Because a continuum is not required, this method can be used to solve problems involving complex geometric boundaries. On the other hand, the LBM is known for its inability to calculate flow over a large area and its limited range of simulation.^{39,40} The LBM simulates the original state and motion of the molecules in a system on a computer and subsequently analyzes the structure and properties of the system to produce many microscopic details that cannot be experimentally obtained, with the goal of revealing the molecular fluid–solid coupling and migration mechanisms. The limitations of this method are that the reliability of its results depends not only on the accuracy of the initial molecular configuration and intermolecular potential but also, to a large extent, on computer capabilities.^{41–47}

A molecular dynamics model of a nanoscale OM slit filled with methane molecules was established to analyze the microscopic mechanisms behind the interactions between the methane molecules and between the methane molecules and the walls of the slit. This model is composed of two carbon plates, each constructed with three graphite layers. The initial graphite lattice originated from the Material Studio software database. The condensed-phase optimized molecular potentials for atomistic simulation studies (COMPASS) force field was applied to the model. A Monte Carlo simulation was first performed to determine the number of methane molecules at certain temperatures and pressures. Subsequently, a molecular dynamics simulation was carried out to identify the stable conformation. On this basis, statistical data for several quantities (e.g., density distribution, interaction energy, diffusion coefficient, and mobility) were obtained. Figure 4 shows the simulation results for gas molecules at different pressures (1, 11, 21, 31, and 41 MPa) and slit lengths L (1, 2, 3, 5, and 10 nm). A macroscopic seepage model was established to provide a basis for identifying the mechanism behind the distribution of gas.

Our analysis of the molecular density and velocity profiles (Figure 3a) reveals the following. The density of methane molecules varies considerably across the 2 nm pore due to the wall effects. Some methane molecules are clustered near the walls, resulting in the appearance of an adsorption peak. The density of molecules near the walls of the slit is substantially higher than the density of free gas molecules at its center. The

densities of free gas molecules at the center of the nanoscale slit under different pressures are consistent with the corresponding values in the database provided by the U.S. National Institute of Standards and Technology,⁴⁸ lending credence to the soundness of the molecular dynamics simulation. As the pressure increases, the peak density corresponding to the adsorption peak increases gradually but at a decreasing rate. As the pressure increases beyond 11 MPa, a second peak emerges between the peak and bulk densities. This finding echoes the observation of Mosher et al.⁴⁸ and can be ascribed to the following factor. The gas molecules responsible for the formation of the adsorption peak near the walls exert an additional adsorptive force on their neighboring gas molecules, resulting in a small dense gas zone between the area corresponding to the adsorption peak and the free gas molecules. In other words, a “dual adsorption mechanism” is behind the distribution of the gas in the nanoscale slit.⁴⁹ An observation of the velocity curves shows that the velocity of the molecules fluctuates due to their random motion and decreases as the pressure increases. The spatial motion of the molecules is captured based on their diffusion coefficient to characterize the average mean square displacement of each molecule and the system within the given time period. The self-diffusion coefficient of the molecules is set to the literature values,⁴⁵ ranging from 4.09×10^{-8} to $4.94 \times 10^{-7} \text{ m}^2 \cdot \text{s}^{-1}$ under the conditions used in the analysis, and it decreases at a decreasing rate as the pressure increases.

Figure 3b shows the simulation results for the gas in the slit-shaped pore at different L values (1, 2, 3, 5, and 10 nm). The methane is distributed in a layered pattern in the slit at $L > 2$ nm. In other words, under this condition, more methane molecules accumulate in the adsorption layers near the walls than at the center. In contrast, at $L = 1$ nm, the density of adsorbed methane molecules is considerably greater than that of free methane molecules almost across the entire pore, which can be primarily attributed to the action of the superposed force at the wall on each side of the pore.⁵⁰ This force results in an overall increase in the adsorptive force, which in turn increases the density of methane molecules and immediately induces adsorption. Consequently, the pore is devoid of areas containing free molecules. Hence, a material containing a large number of micropores generally has a very high adsorptive capacity.^{51–54} In the absence of the application of a force field to the walls, the area under the influence of the microscale effects is within approximately 0.65 nm from the wall on each

side of the slit. Thus, it is inferred that the threshold pore width at which all the gas molecules are affected by the microscale effects is between 1 and 2 nm under the conditions used for analysis. Within this range, the mass transport of the gas in the pore occurs primarily through Knudsen and surface diffusion. Outside this range, the flow of the free gas molecules follows Darcy's and Fick's laws. This finding lays a theoretical foundation for modeling gas flows in pores of different sizes and under different pressures.

Gas Flowability Characterization Model. Unlike a single-tube model, a shale core consists of pores of various sizes, resulting in the coexistence of multiple flow mechanisms, such as Darcy flow, bulk diffusion, Knudsen diffusion, and surface diffusion. This condition precludes the use of the conventional Darcy permeability intrinsic permeability (K_D) to characterize gas flowability in cores. Hence, in many studies, multiple flow mechanisms are comprehensively combined into an apparent permeability (K_a) model.^{55,56} Some examples of K_a models include the apparent permeability (K_a) models developed by Jones and Owens⁵⁶ and Florence et al.⁵⁷ based on the static slippage factor, the K_a models developed by Ertekin et al.⁵⁸ and Michel et al.⁵⁹ through the introduction of a dynamic slippage factor to account for Knudsen diffusion, the Knudsen number (Kn)-containing K_a models developed by Sakhaee-Pour and Bryant⁶⁰ and Civan et al.⁶¹ based on the work of Beskok and Karniadakis,⁶² and the expression of K_a established by Javadpour et al.^{63–65} that accounts for diffusive flow (Knudsen diffusion) and the slip effect. Most of these K_a models are functions of the Kn or gas pressure. K_a estimates yielded by different methods differ relatively considerably as the pressure and pore size vary,^{55,66} which is primarily due to the unclearly defined boundary of the interaction between the microscopic mechanisms of shale gas in each model. Analysis of molecular dynamics simulations reveals that both the slip effect and Knudsen diffusion involve molecule–wall collisions. However, in many studies,^{62,63,67} various transport mechanisms are directly linearly coupled to produce a combined transport model. This approach results in double counting of the flow. In addition, these models are composed of microtubes with an identical diameter, while the effects of the presence of different pore sizes on gas flow in cores are rarely considered. As a result, estimates produced by these models differ substantially from the actual flow.⁶⁸

According to the results of the molecular dynamics simulations, the flow region is divided into boundary flow and bulk flow. Four flow mechanisms need to be considered: the viscous flow and bulk diffusion in the bulk flow and the surface diffusion and Knudsen diffusion that result in nonzero gas velocities near the wall under the action of the forces exerted by the gas and solid phases.⁶⁹ The pore space in a core sample can be made equivalent to an amalgamation of cylindrical capillaries with different diameters. Here, the flow in a single cylindrical tube is examined. Let r_{in} be the internal flow radius of the tube. As a result of the adsorption effects of the wall, the boundary layer (i.e., the adsorption layer) occupies a certain proportion of the pore space. The equivalent internal radius of the single tube that accounts for the effects of the adsorption layer, r_{ine} , is given below:⁶⁸

$$r_{ine} = r_{in} - h_e = r_{in} - \frac{pd_m}{p_L + p} \quad (1)$$

where d_m is the diameter of the gas molecule, nm; h_e is the equivalent adsorption-layer thickness at a pressure of p , nm; p_L is Langmuir pressure, MPa; P is the formation pressure in the reservoir, MPa; r_{ine} denotes equivalent internal radius accounting for the effects of adsorption, nm; and r_{in} denotes equivalent internal radius of the single tube, nm.

Therefore, the mass flow rate of the viscous flow, N_D , can be expressed as follows:⁹

$$N_D = -\frac{10^{-36}\pi\rho_{avg}}{8\mu} \left(r_{in} - \frac{pd_m}{p_L + p} \right)^4 \nabla p \quad (2)$$

where N_D is the mass flow rate of viscous flow, $\text{kg}\cdot\text{s}^{-1}$; ρ_{avg} is gas density at the inlet and outlet at the average pressure, $\text{kg}\cdot\text{m}^{-3}$; ∇p is pressure gradient, $\text{Pa}\cdot\text{m}^{-1}$; and μ is gas viscosity, $\text{Pa}\cdot\text{s}$.

Because bulk diffusion follows Fick's law of diffusion, the bulk diffusion flux that accounts for the effects of the adsorption layer has the following expression:

$$N_F = -\frac{10^{-9}Mk_B}{3R\mu d_m} \left(r_{in} - \frac{pd_m}{p_L + p} \right)^2 \nabla p \quad (3)$$

where N_F is the mass flow rate of Fick's diffusion, $\text{kg}\cdot\text{s}^{-1}$; k_B is the Boltzmann constant ($1.38 \times 10^{-23} \text{ J}\cdot\text{K}^{-1}$); M is molecular weight, $\text{kg}\cdot\text{mol}^{-1}$; and R is the universal gas constant ($8.314 \text{ J}\cdot\text{mol}^{-1}\cdot\text{K}^{-1}$).

The Knudsen diffusion in a nanopore can be expressed in terms of a function of the pressure gradient. Thus, the mass flow rate of the Knudsen diffusion is as follows:^{66,70}

$$N_K = -\frac{2 \times 10^{-27}}{3} \left(\frac{8\pi M}{RT} \right)^{0.5} \left(r_{in} - \frac{pd_m}{p_L + p} \right)^3 \nabla p \quad (4)$$

where N_K is the mass flow rate of Knudsen diffusion, $\text{kg}\cdot\text{s}^{-1}$, and T is ambient temperature, K.

Sladek et al.⁷⁰ derived the following equation for the surface diffusion coefficient through fitting to data for gas–solid systems:

$$D_s = 0.016 \times 10^{-4} \times \exp\left(-\frac{0.45q}{mRT}\right) \quad (5)$$

where D_s is the surface diffusion coefficient, $\text{m}^2\cdot\text{s}^{-1}$; m is a constant determined based on the type of adsorption bond, dimensionless; and q is isosteric heat of adsorption, $\text{J}\cdot\text{mol}^{-1}$.

It is assumed that the separated circular cross-sectional area of a single capillary is directly proportional to the ratio of the volume of the capillary to the total pore volume. The flow flux commonly used for surface diffusion refers to its flow rate divided by the circular cross-sectional area. On this basis, the mass flow rate of the surface diffusion in a single capillary is obtained as follows:

$$N_s = -0.016 \times 10^{-22} \times \exp\left(-\frac{0.45q}{RT}\right) \frac{\rho_s M}{pV_{std}} \frac{q_L p}{p_L + p} \frac{1 - \phi_{co}}{\phi_{co}} \pi r_{in}^2 \nabla p \quad (6)$$

where N_s is the mass flow rate of surface diffusion, $\text{kg}\cdot\text{s}^{-1}$; ρ_s is shale matrix density, $\text{kg}\cdot\text{m}^{-3}$; V_{std} is the molar volume of the gas in a standard state, $\text{m}^3\cdot\text{mol}^{-1}$; and ϕ_{co} is the porosity of the core sample, dimensionless.

Because the surface diffusion of shale gas occurs primarily in the adsorption layer, r_{in} is used in eq 6. To prevent double counting of the flow caused by direct superposition, a coupling coefficient for each of the viscous flow, bulk diffusion, Knudsen diffusion, and surface diffusion ($f_1(Kn)$, $f_2(Kn)$, $f_3(Kn)$, and $f_4(Kn)$, respectively) is used. These coefficients are all functions of the Kn . The flow rate in a nanotube at a specific Kn is expressed as follows:

$$N = f_1(Kn)N_D + f_2(Kn)N_b + f_3(Kn)N_K + f_4(Kn)N_s \quad (7)$$

where $f_1(Kn)$ is the coupling coefficient for viscous flow, dimensionless; $f_2(Kn)$ is the coupling coefficient for bulk diffusion, dimensionless; $f_3(Kn)$ is the coupling coefficient for Knudsen diffusion, dimensionless; $f_4(Kn)$ is the coupling coefficient for surface diffusion, dimensionless; N is the mass flow rate of the gas in a single tube, $\text{kg}\cdot\text{s}^{-1}$; and Kn is Knudsen number, dimensionless.

Based on earlier studies,^{71,72–74} Liu⁴⁷ gave the following definition for each of these four coupling coefficients: $f_1(Kn) = e^{-\alpha Kn}$, $f_2(Kn) = 1/(1 + Kn) - e^{-\alpha Kn}$, $f_3(Kn) = e^{-\beta/Kn}$, and $f_4(Kn) = Kn/(1 + Kn) - e^{-\beta/Kn}$ (α and β are constants to be calculated). On this basis, the convexity of the curve depicting the variation in each coupling coefficient can be determined. Similarly, a curve depicting the variation in each coupling coefficient with Kn at $\alpha = 5$ and $\beta = 1.8$ was obtained through calculations, as shown in Figure 4.

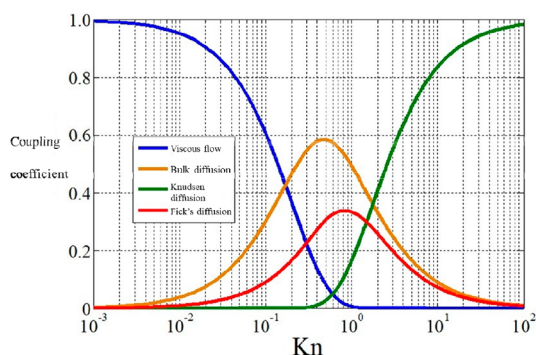


Figure 4. Variation in the coupling coefficients with Kn .

Our observation of Figure 4 shows the following. Because $f_1(Kn)$, $f_2(Kn)$, $f_3(Kn)$, and $f_4(Kn)$ are all nonnegative, they are applicable within the Kn range of $[0, \infty]$, thereby evading the necessity for solving the flow model in a piecewise manner. In addition, the coupling coefficients vary smoothly and gradually, and thus the required smooth transition of viscous flow and each type of diffusion with Kn is satisfied. The unified flow model bridges the boundaries between the flow patterns and eliminates the jumps of the flow rates at the flow-pattern transition points. A normalized correspondence between the flow mechanisms and Kn is used to sufficiently reflect the basic understanding of the flow patterns, thereby further constraining the range of action in the mathematical model. Substituting the expression of each coupling coefficient into eq 7 yields

$$N = e^{-5Kn}N_D + \left(\frac{1}{1 + Kn} - e^{-5Kn} \right) N_F + e^{-1.8/Kn}N_K + \left(\frac{Kn}{1 + Kn} - e^{-1.8/Kn} \right) N_s \quad (8)$$

The above equation calculates the mass flow rate in a single-tube model. A core sample can be made equivalent to a combination of single-tube models of various sizes. According to the studies of Michel et al.⁷⁴ and Xiong et al.,⁷⁵ the pore-size distribution in a porous medium can be described with a log-normal function. Based on the characteristics of the full-range pore-size distribution curve of shales, experimental data for the full-range pore-size distribution in shales are fitted to a log-normal function. Thus, a probability density function of the pore size distribution is obtained. Averaging the parameters yields the following generalized curve:

$$f(r_{in}) = \frac{1}{0.9060r_{in}\sqrt{2\pi}} e^{-0.5\left(\frac{\ln r_{in} - 0.8055}{0.9060}\right)^2} \quad (9)$$

The number of tubes (i.e., pores) with an internal radius that ranges from r_{in} to $(r_{in} + dr_{in})$ in a shale core is as follows:

$$N = \frac{10^{18}\phi_{co}V_{co}}{\pi r_{in}^2 L_{co}} f(r_{in}) dr_{in} \quad (10)$$

where V_{∞} is the external surface volume; L_{∞} is the length; and Φ_{∞} is the porosity.

Integrating eq 10 over the entire pore-size range yields the flow rate in the shale medium:

$$Q = \int_{r_{in,min}}^{r_{in,max}} \left\{ 10^{18} \left[e^{-5Kn}N_D + \left(\frac{1}{1 + Kn} - e^{-5Kn} \right) N_F + e^{-1.8/Kn}N_K + \left(\frac{Kn}{1 + Kn} - e^{-1.8/Kn} \right) N_s \right] \phi_{co} V_{co} \right\} / (\pi r_{in}^3 L_{co} \sigma \sqrt{2\pi}) e^{-0.5\left(\frac{\ln r_{in} - \eta}{\sigma}\right)^2} dr_{in} \quad (11)$$

where η is normal mean, dimensionless; L_{co} is length of the core sample, m; V_{co} is volume of the core sample, m^3 ; and Φ_{co} is porosity of the core sample, dimensionless.

Flow Experiment and Model Validation. A steady-state flow test setup developed in-house was used to analyze the gas-shale apparent permeability (K_a) and flowability of shale gas at pressures of 0.1–40 MPa to achieve two objectives: (1) to better analyze the pattern of variation in the flow rate in a core under the combined action of multiple flow mechanisms and (2) to provide experimental evidence and data support for validating the established shale gas flowability evaluation model. Figure 5 shows the obtained K_a – K_D (intrinsic permeability) ratios for cores with different permeabilities at different pressures.

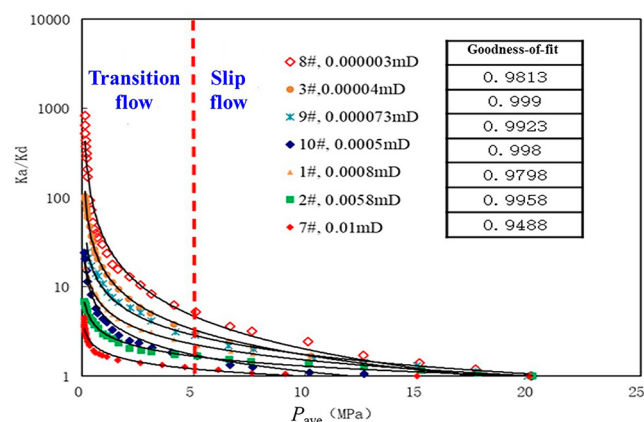


Figure 5. K_a – K_D ratios at different pressures.

Observation of the flow–pattern curves at different pressures shows the following. K_a increases considerably as the average pressure P_{ave} decreases. The K_a – K_D ratio increases nearly linearly and slowly as P_{ave} decreases before reaching 5 MPa. Within this range, the overall increase in the K_a – K_D ratio is less than 1 order of magnitude, while the characteristics of each flow–pattern curve are consistent with those of the curve of a slip flow pattern. As P_{ave} decreases below 5 MPa, the flow pattern gradually transitions from a slip flow pattern to a transition flow pattern. A decrease in P_{ave} increases the length of the free path of molecules and consequently strengthens the Knudsen diffusion, which in turn results in an exponential increase in the dimensionless permeability (i.e., the ratio of K_a to the absolute permeability). A low level of permeability leads to a high dimensionless permeability. Lowering the pressure can increase the dimensionless permeability 1- to 10-fold and 10- to 100-fold for micro- and nano-Darcy cores, respectively.^{76–78}

Compared to other models,⁷⁹ the model developed by our group to evaluate gas flowability in the matrix accounts for different microscopic mechanisms of action, and consequently, its estimates for low- and high-pressure conditions are the closest to the experimental results (Figure 6). Therefore, this model can provide a basis for estimating gas flowability in reservoirs and evaluating the development potential of gas wells.

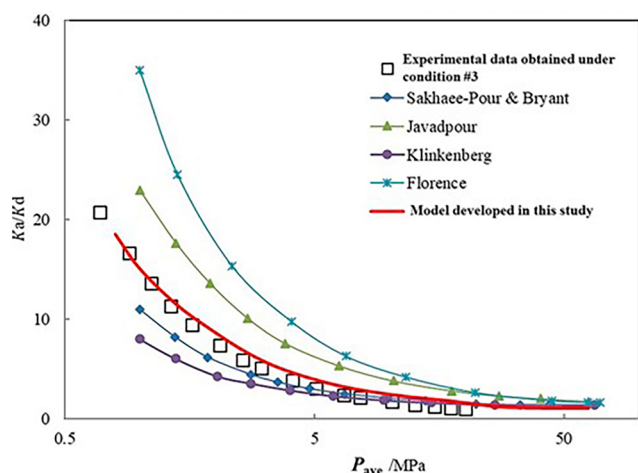


Figure 6. Comparison of K_a – K_D ratios yielded by different models.

DEVELOPMENT SIMULATION EXPERIMENT AND COUPLED SEEPAGE MODEL

Simulation of Full-Life-Cycle Depletion-Mode Development. Micro- and nanopores and unique transport mechanisms are present in shale reservoirs. As a result, shale gas wells are known for high initial production, followed by a fast decline and a long period of low but stable production at the final stage. Currently, analysis based on gas-well production data is often affected by production systems and engineering factors. The associated problems (e.g., discontinuous production data and pressure) are detrimental to the dynamic analysis of gas-well development.^{80,81} Establishing corresponding physical development simulation methods can help to produce complete production data and some key parameters essential to numerical simulations,^{82,83} thereby addressing the current

challenge of acquiring data required for gas-well productivity estimations and dynamic production predictions.

A development simulation test setup developed in-house for full-diameter core samples was used to simulate the development pattern of a full-diameter core sample over its full life cycle. With a length of 15 cm, a diameter of 10 cm, and a porosity of 2.5%, this sample was retrieved in sealed conditions from the LMX Fm in Zhaotong in southern Sichuan. After being transported to the laboratory, the sample was replenished with methane until its pressure reached the in situ level (30 MPa). Subsequently, a full-life-cycle development process in depletion mode (used in situ) was dynamically simulated. The test setup included a high-pressure core clamping system, a gas collection system, a pressure measurement system, and a temperature control system. During the test, the inlet and outlet pressure (P_{in} and P_{out} , respectively) and the flow rate at the outlet (R_{out}) were continuously recorded in real time using a pressure sensor and a gas mass flowmeter, respectively. As of the preparation of this report, gas had been produced from the full-diameter shale core for over 2700 days. Figure 7 shows the variation in P_{in} and R_{out} with time.

Observation of the gas production and pressure curves (Figure 8) reveals the following. Gas production was high at the initial stage but declined rapidly, which was quickly followed by a steady production stage. The production decline curve is highly similar to the single-well production decline curve and displays an L-shaped pattern. The extraction of the free gas was responsible for the high production at the initial stage. The subsequent extraction of the adsorbed gas propelled the production into a steady stage. The physical simulation satisfactorily reflects the characteristics of shale gas production—an initial high level of production, followed by a fast decline and subsequently a steady level of production at the later stage.^{81,85}

Analysis of the apparent formation pressure–cumulative gas production curve (Figure 8) reveals that the depletion-mode shale gas development process involved approximately three stages. During the high-speed development stage that occurred in the first 40 days, the gas production rate declined rapidly, while the apparent formation pressure did not change significantly and remained greater than 20 MPa. Almost all the gas produced during this stage was in the free state. During the medium-speed development stage that occurred between the 40th and 440th days, the gas production rate declined slowly, while the apparent formation pressure decreased relatively substantially and linearly as the cumulative gas production increased. In addition, during this stage, the average formation pressure decreased to 14.78 MPa, and desorbed gas accounted for a small proportion of the gas produced from the core sample. During the long-term, low-speed steady development stage that occurred between the 440th and 1700th days, the gas production rate remained stable and declined extremely slowly, while the apparent formation pressure decreased at a markedly decreasing rate and basically linearly as the cumulative gas production increased. At the end of the time period examined, the apparent formation pressure decreased to 9 MPa, while the proportion of the produced gas that was in the adsorbed state became increasingly higher. The material balance method was employed to calculate the production patterns and contribution rates for adsorbed and free gas. Our analysis of the results, shown in Figure 9, further identifies adsorbed gas as an

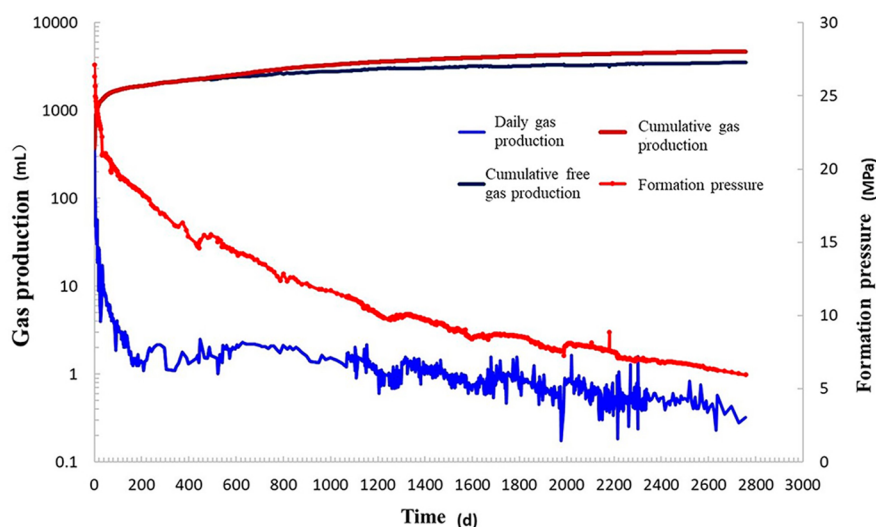


Figure 7. Experimental production decline curves of the full-diameter core.

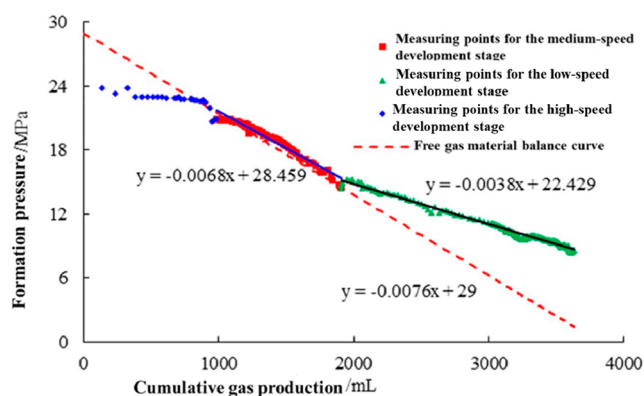


Figure 8. Apparent formation pressure–cumulative gas production curve for the core over the full life cycle.

The gas production patterns of a certain shale gas well Changing at different production times were analyzed based on its actual production data in conjunction with the production decline patterns for adsorbed and free gas obtained from the laboratory full-life-cycle depletion-mode development simulation experiment on a physical model (Figure 9). On average, this well produces 108,000 m³ of gas every day during the first year. Over time, gas production from this well decreases rapidly. Specifically, its production decreases to 40,000 m³ of gas every day during the second year, followed by a low-level, steady production stage. The total amount of gas produced during the first three years accounts for more than 50% of the estimated ultimate recovery (EUR). During the first year, free gas accounts for the majority of the gas produced from this well, while the proportion of adsorbed gas is very low (<5%). As the production progresses, the reservoir pressure decreases. Consequently, free gas is extracted in large quantities, accompanied by a gradual increase in the production of adsorbed gas. During the eighth year, the production of adsorbed gas reaches 10,000 m³ per day. At this

important source of shale gas during the later long-term steady production stage.^{81,84}

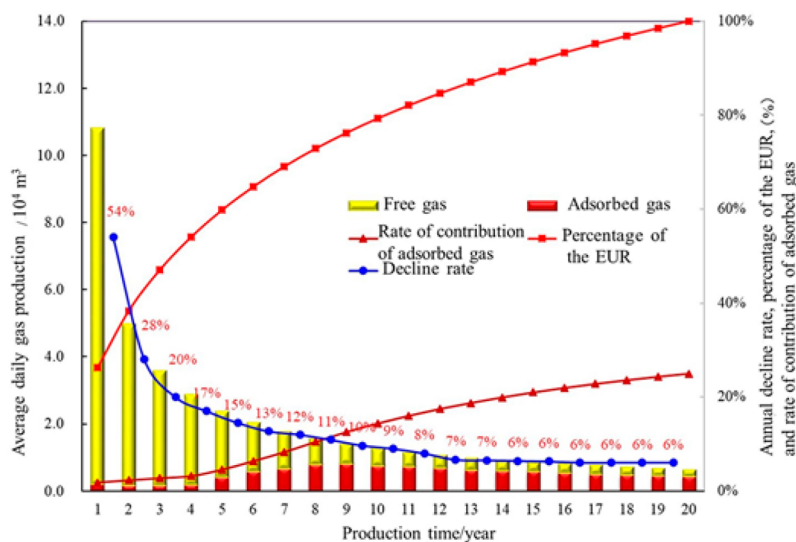


Figure 9. Production decline rates and contribution rates of adsorbed gas at different production times.

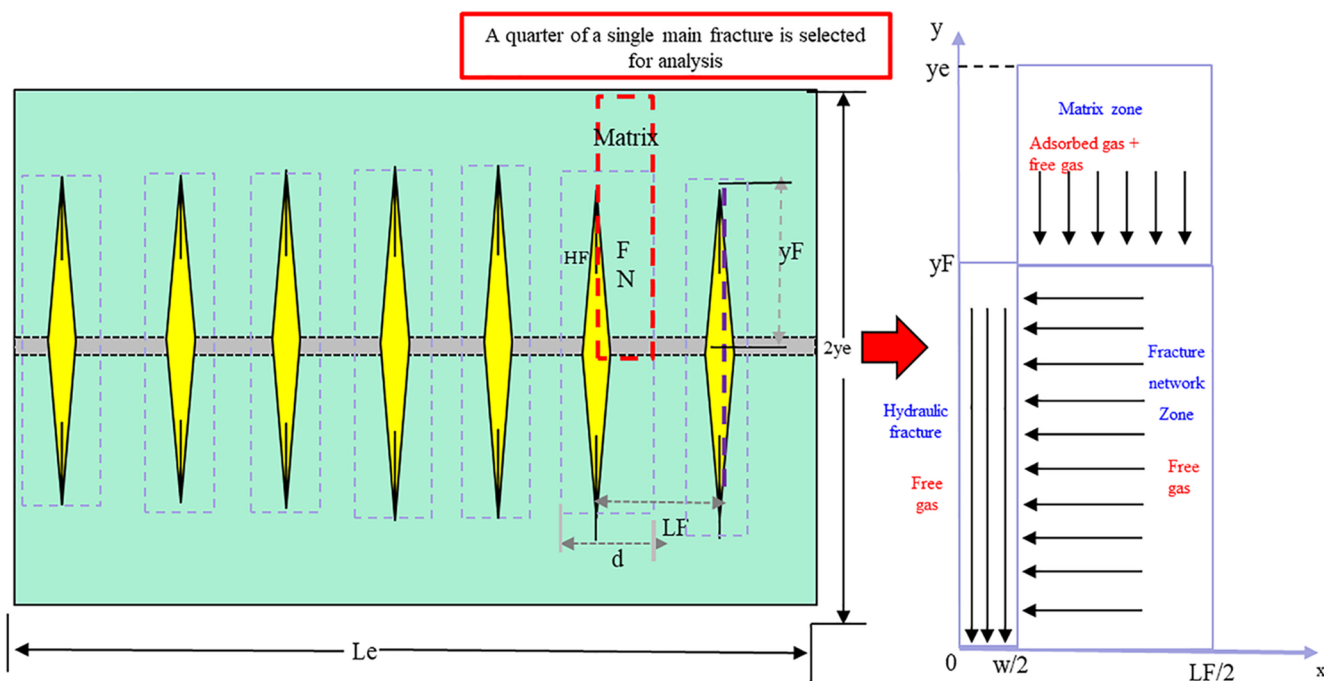


Figure 10. SRV division model: simplified equivalent model of the main fracture, secondary fracture network, and matrix system.

stage, adsorbed gas contributes more than 50% of the total gas produced from the well. As the production further progresses, the rate of contribution of adsorbed gas increases. Analysis of the cumulative rate of contribution of adsorbed gas reveals the following: (1) adsorbed gas accounts for less than 5% of the total gas produced from this well in the first five years and (2) the desorption of adsorbed gas is a primary source of shale gas and is responsible for 25% of the total gas produced from this well at the end of production. Because the production difficulty varies between gases in different states, the free gas–adsorbed gas ratio is another metric that warrants careful consideration in the selection of optimum blocks and horizons for development. A reservoir dominated by free gas has a high-pressure coefficient and produces mostly free gas. A high proportion of free gas results in a high gas production rate and short-term recovery. Adsorbed gas does not play a major role until the pressure in a reservoir dominated by free gas decreases to a low level.^{86–88} In comparison, reservoirs dominated by adsorbed gas are developed primarily through pressure reductions. Although the gas production rates are low, these reservoirs are able to steadily produce gas over a relatively long period of time (on the scale of decades).^{89–92}

Mathematical Model of a Coupled Matrix and Fracture Seepage. Large-scale volumetric fracturing is required to achieve profitable production in shale gas reservoirs. A description of the coupled flow pattern of the gas in the matrix and fractures forms the basis for evaluating the productivity of a shale gas well and producing dynamic predictions for its development. Bello and Wattenbarger,⁹² Ahmadi et al.,⁹³ Brown et al.,⁹⁴ Stalgorova and Mattar,⁹⁵ Zhu et al.,⁹⁶ Gao et al.,⁸⁴ and Duan et al.⁹⁷ studied models that describe coupled shale gas flow in multistage-fractured horizontal wells and predicted productivity. Most of these models account for the effects of the adsorption, desorption, and diffusion of shale gas on seepage. However, some models fail to comprehensively consider the effects of three aspects of the gas—its physical properties under high pressures, super-

critical desorption characteristics, and multiple micro- and nanoscale flow mechanisms—on gas-well production patterns.

An improved variant of the conventional trilinear flow model was established through comprehensive consideration of the effects of the high-pressure physical properties, supercritical adsorption, and multiple nonlinear flow mechanisms of gas in addition to the stress sensitivity of gas reservoirs. On this basis, a semianalytical estimate for productivity was obtained, and its reliability was examined through a case study. This model divides the stimulated reservoir volume (SRV) into two regions—an internal region and an external region—as shown in Figure 10. The internal region contains symmetrical, equal-length artificial fractures distributed uniformly along the horizontal well. A large number of natural fractures and a network of secondary fractures are present in the reservoir areas between the artificial fractures. The reservoir gas in these areas is extensively extracted. The external region refers to the matrix region unaffected by artificial fracturing. The matrix only unidirectionally supplies gas to the fractures in the internal region. The gas in the fracture network flows into the artificial fractures under the action of the pressure gradient and then is subsequently directed to the well shaft by the artificial fractures. The effects of the diffusion and slip of free gas in micro- and nanopores are considered in the analysis of the gas flow in the matrix and are subsequently integrated into the K_a model for shale gas. Based on flow conductivity, the internal region is further divided into two subregions. The gas in the fracture network, consisting only of free gas, flows linearly to the main fracture. Considering this factor in conjunction with the effects of stress sensitivity on flowability, the gas flow in the main fracture can be characterized using Darcy's law.^{98–100}

Matrix in the external region: The gas in the matrix in the external region moves in the y -direction in an unsteady cross-flow pattern into the fracture network in the internal region. Considering the supercritical desorption, diffusion, and slip of the gas, the external boundary is sealed, while a continuous pressure is applied to the internal boundary. Application of the

law of conservation of mass yields the following governing equation for seepage in the matrix:

$$\frac{\partial(\rho_g \Phi_m)}{\partial t} + \frac{\partial(1 - \Phi_m)q_{ad}}{\partial t} = -\frac{\partial}{\partial y}(\rho_g v_m) \quad (12)$$

where ρ_g is gas density, kg/m³; Φ_m is matrix porosity, dimensionless; t is production time, s; q_{ad} is supercritical excess adsorption of shale gas per unit matrix volume, kg/m³; and v_m is the gas flow rate in the matrix, m/s.

The supercritical adsorption model corrected for the excess of shale gas,^{67,101} shown below, is employed to better evaluate the adsorption and desorption characteristics of methane in a high-temperature, high-pressure reservoir.

$$q_{ad} = \frac{P_{sc}M}{Z_{sc}RT_{sc}} V_L \frac{P_m}{P_m + P_L} \left(1 - \frac{\rho_g}{\rho_a} \right) \quad (13)$$

where P_{sc} is standard atmospheric pressure at ground level (0.101 MPa); T_{sc} is temperature in the standard state (273.15 K); Z_{sc} is compressibility factor for an ideal gas, dimensionless; ρ_a is the density of the adsorbed phase, kg/m³; and P_m is gas pressure in the matrix pore, Pa.

The gas seepage velocity in the matrix can be derived from the equation of motion:

$$v_m = -\frac{K_{ma}}{\mu_m} \frac{\partial P_m}{\partial y} \quad (14)$$

where K_{ma} is matrix apparent permeability, m², and μ_m is gas viscosity, Pa·s.

Javadpour's K_a model⁶⁵ is used to characterize the diffusion and slip of the gas in the nanopores in the matrix:

$$K_{ma} = c_g D \mu + F K_m \quad (15)$$

where c_g is gas compressibility, Pa⁻¹; D is gas diffusion coefficient, m²/s; K_m is matrix intrinsic permeability, m²; and F is slippage factor, dimensionless, where F is the slippage velocity correction factor and can be calculated as follows:

$$F = 1 + \sqrt{\frac{8\pi RT}{M} \frac{\mu_m \times 10^{-3}}{P_m \times 10^6 r} \left(\frac{2}{\alpha} - 1 \right)} \quad (16)$$

where α is the tangential moment accommodation coefficient, which depends on factors such as the smoothness of the internal wall of the pore, gas type, temperature, and pressure (range: 0–1; set to 0.8), and r is pore initial radius, m.

The following gives the expression of the hydraulic flow diameter r_m

$$r_m = \sqrt{\frac{8K_m}{\Phi_m}} \quad (17)$$

Boundary conditions take the form of eqs 18~20.

Initial conditions:

$$P_m(t = 0) = P_e \quad (18)$$

where P_e is the initial reservoir pressure, Pa.

Outer boundary:

$$\left. \frac{\partial P_m}{\partial y} \right|_{y=y_e} = 0 \quad (19)$$

where y_e is well spacing, m.

Inner boundary:

$$P_m(y = y_f) = P_f(y = y_f) \quad (20)$$

where y_f is half fracture length, m, and P_f is gas pressure in the fracture network, Pa.

Considering the impact of stress sensitivity on gas viscous flow in the fracture network zone, the flow rate on the outer boundary between the matrix and fracture network is continuous, and the pressure on the inner boundary is continuous.

An exponential stress sensitivity empirical model¹⁰¹ is adopted in this paper to characterize the impact of the stress sensitivity of secondary fracture on gas flow, which is expressed in eq 21:

$$K_f = K_{fi} e^{-\gamma(P_c - P_f)} \quad (21)$$

where K_f is fracture permeability accounting for stress sensitivity, m²; K_{fi} is intrinsic permeability of the fracture system, m²; and γ is stress sensitivity coefficient, Pa⁻¹.

The gas flow equation in the fracture network can be depicted in eq 22:

$$\frac{\partial(\rho_g \Phi_f)}{\partial t} = \frac{\partial}{\partial x} \left(\rho_g \frac{K_f}{\mu_f} \frac{\partial P_f}{\partial x} \right) + 2\rho_g \frac{K_m}{\mu_m y_f} \frac{\partial P_m}{\partial x} \Big|_{y=y_f} \quad (22)$$

where Φ_f is the fracture network porosity, dimensionless.

The boundary conditions are as follows in eqs 23–25).

Initial condition:

$$P_f(t = 0) = P_e \quad (23)$$

Outer boundary:

$$P_f(x = 0) = P_f(x = l) \quad (24)$$

where P_f is gas pressure in the hydraulic fracture, Pa.

Inner boundary:

$$\left. \frac{\partial P_f}{\partial x} \right|_{x=d/2} = \frac{K_m}{K_f} \frac{\partial P_f}{\partial y} \Big|_{x=d/2} \quad (25)$$

where d is the stimulated width of a fracture network, m.

The gas flow in the hydraulic fracture is linear flow, and gas flow governing eq 26 in the hydraulic fracture is established:

$$\frac{\partial \rho_g \Phi_F}{\partial t} = \frac{\partial}{\partial y} \left(\rho_g \frac{K_F}{\mu_F} \frac{\partial P_F}{\partial y} \right) + 2 \frac{\rho_g K_f}{\mu_F L_F} \frac{\partial P_f}{\partial x} \Big|_{x=d/2} \quad (26)$$

where Φ_F is hydraulic fracture porosity, dimensionless; K_F is intrinsic permeability of hydraulic fracture, m²; μ_F is gas viscosity in hydraulic fracture, Pa·s; and L_F is hydraulic fracture spacing, m.

Considering the constant bottom hole pressure of the gas well and that the outer boundary is closed, the initial and boundary conditions are as follows.

Initial condition:

$$P_f(t = 0) = P_e \quad (27)$$

Outer boundary:

$$\left. \frac{\partial P_F}{\partial t} \right|_{y=y_f} = 0 \quad (28)$$

Inner boundary:

$$P_F(y = 0) = P_{wf} \quad (29)$$

where P_{wf} is the bottom hole pressure, Pa.

Laplace transformation can be first be adopted to get the dimensionless production solution in the Laplace space. Then based on the Stehfest numerical inversion,¹⁰² the semi-analytical solution of the dimensionless production in real space is obtained. In the end, combining with the Newton iteration method, the production solution in the real space at constant pressure can be derived.

Here, a multistage-fractured horizontal well in the Weiyuan Shale Gas Demonstration Area is used as an example for illustration purposes. Table 1 summarizes the relevant

Table 1. Geological Parameters of the Reservoir and Parameters of the Horizontal Well

parameter	value	parameter	value
Initial formation pressure/MPa	45	Number of fractured sections	25
Formation temperature/K	392.4	*Fracture half-length/m	80
Reservoir thickness/m	30	*Main fracture width/m	0.003
Matrix porosity/%	3.5	External boundary length/m	300
Matrix permeability/mD	3.629×10^{-4}	Horizontal well length/m	1500
*Microfracture porosity	5.6	Bottomhole flowing pressure/MPa	5
*Microfracture permeability/mD	6.529×10^{-3}	Rock density/(kg/m ³)	2600
Main fracture permeability/mD	10	Pressure sensitivity factor for the fracture network/MPa ⁻¹	0.13
Langmuir volume/(m ³ /t)	3.7	Langmuir pressure/MPa	9.05
Reservoir compressibility factor/MPa ⁻¹	8.78×10^{-4}	Number of fracture clusters	3

geological and well-completion parameters, which refer to common parameter-value ranges used in operation sites for gas shale. The semianalytical model developed earlier was used to fit the dynamic production data for this well by adjusting the parameters with high uncertainty at its appropriate distribution range and to estimate its EUR (* indicates a model-fitted parameter).

Observation of the fit for the single well in Figure 11 reveals the following. (1) The model considers the contribution of the real-world high-pressure gas adsorption and multiple microscopic non-Darcy effects in the reservoir on production. (2) There is a high goodness-of-fit between the model-generated data and the actual production data. (3) The model is able to produce accurate estimate of the recoverable reserves and recovery for the gas well. Calculations obtained using this model show a 20-year cumulative production of 1.24×10^8 m³ of gas for this gas well. Our analysis of Figure 12 shows a significant impact of supercritical adsorption on gas production from this well during the later stage. This finding is consistent with that obtained from the development simulation experiment. In real-world production, the effects of supercritical adsorption cannot be overlooked because failure to do so can result in underestimating the productivity and recovery. Similarly, the effects of nonlinear gas flow on gas-well productivity are also a nonnegligible factor. Compared to diffusion, the slip effect contributes more considerably to

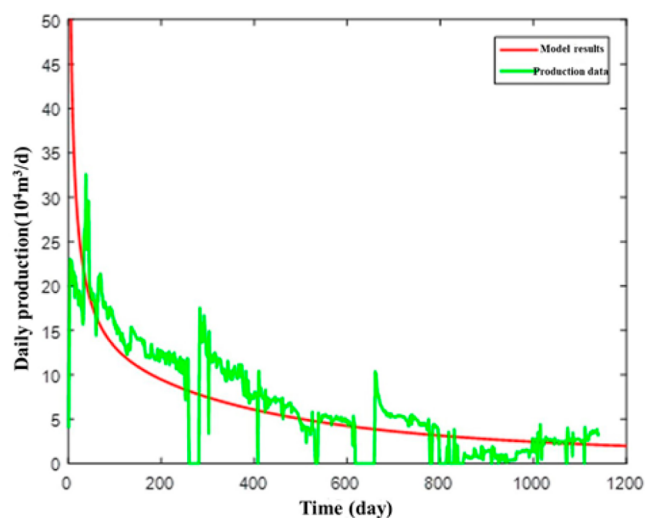


Figure 11. Analysis of the fit for the single well.

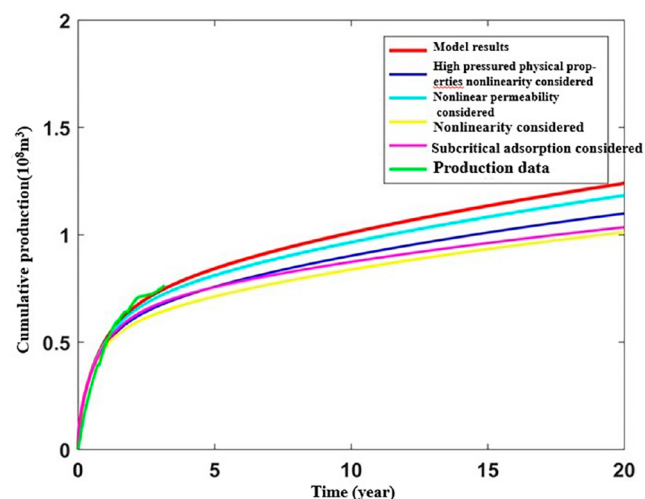


Figure 12. Estimated EUR for the single well.

production as it leads to a gentle decline in daily gas production and a higher corresponding output, which can be ascribed to the following factor. The overall pressure in a shale reservoir decreases during the later stage of production. Under a low pressure, nonlinear mechanisms (e.g., gas desorption and diffusion) in the matrix of the shale reservoir become more pronounced, resulting in significantly increased flowability. Neglecting the nonlinear effects of shale gas in the reservoir matrix can lead to an underestimate of the productivity of the shale gas well.

CONCLUSION

The shale gas production in reservoirs can be attributed to the micro- and nanoscale pore space that stores shale gas and to varying flow mechanisms. First, micro- and nanopores were characterized to clarify the full-range pore-size distribution in shale reservoirs. Pores smaller than 50 nm in diameter were found to account for more than 70% of all the pores and are regarded as the primary space containing adsorbed gas. Molecular dynamics simulations were performed to examine the microscopic mechanism for the distribution of shale gas with different occurrence states. The thickness of the adsorption layer in an OM nanopore was calculated to range

from 0.6 to 0.7 nm. Desorption and diffusion were identified as major mass transport mechanisms in the pores of the shale matrix. A mathematical method that accounts for the microscopic distribution and porous media characterization was established to analyze gas flowability in shale reservoirs, which addresses the limitations of Darcy's law often applied in the conventional reservoirs to characterize gas flowability in shale reservoirs.

Analysis of the results produced by the long-term production physical simulation and coupled flow model established by our group reveals that free gas accounts for most of the gas produced during the early stage of extraction from a shale matrix and that the ratio of adsorbed gas to the total production gradually increases as the pressure decreases. Calculation results for a certain gas well show that the amount of gas produced from this well in the first three years accounted for more than 50% of EUR and that adsorbed gas contributed more to the annual production than free gas in the eighth year. The extraction of adsorbed gas was a principal factor responsible for stable shale gas production during the later stage. Therefore, it is recommended to shorten the distance that the gas supplied by the matrix travels, reduce the fracture pressure, and increase the effective pressure gradient, with the goal of effectively controlling free gas and efficiently extracting adsorbed gas. Our relevant theoretical models and innovative understanding formed based on a series of unique experimental techniques in various areas (e.g., the microscopic evaluation, the coupled multiple flow mechanisms, and production patterns during depletion-mode production) can provide a theoretical basis and scientific guidance for further improving production and recovery from shale reservoirs.

■ ASSOCIATED CONTENT

SI Supporting Information

The Supporting Information is available free of charge at <https://pubs.acs.org/doi/10.1021/acsomega.2c05789>.

Derivation process of the productivity model for the shale gas reservoir (PDF)

■ AUTHOR INFORMATION

Corresponding Author

Yingying Xu – University of the Chinese Academy of Sciences, Beijing 100493, China; orcid.org/0000-0001-8224-2342; Email: xuyingying01@petrochina.com.cn

Authors

Zhiming Hu – Research Institute of Petroleum Exploration and Development, PetroChina, Beijing 100083, China

Xianggang Duan – Research Institute of Petroleum Exploration and Development, PetroChina, Beijing 100083, China

Jin Chang – Research Institute of Petroleum Exploration and Development, PetroChina, Beijing 100083, China

Xiaowei Zhang – Research Institute of Petroleum Exploration and Development, PetroChina, Beijing 100083, China

Shangwen Zhou – Research Institute of Petroleum Exploration and Development, PetroChina, Beijing 100083, China; orcid.org/0000-0003-0426-9683

Rui Shen – Research Institute of Petroleum Exploration and Development, PetroChina, Beijing 100083, China

Shusheng Gao – Research Institute of Petroleum Exploration and Development, PetroChina, Beijing 100083, China

Ying Mu – University of the Chinese Academy of Sciences, Beijing 100493, China

Complete contact information is available at: <https://pubs.acs.org/doi/10.1021/acsomega.2c05789>

Notes

The authors declare no competing financial interest.

■ ACKNOWLEDGMENTS

This research was funded by the Research on New Techniques and Methods of Shale Gas Experimental Testing (Grant No. 2021DJ1905).

■ REFERENCES

- (1) Zhao, W. Z.; Jia, A. L.; Jiao, F. Z. Theoretical insights, core technologies and practices concerning “volume development” of shale gas in China. *Nat. Gas Ind. B* **2019**, *6* (6), 525–538.
- (2) Qiu, Z.; Zou, C.; Wang, H.; Dong, D.; Lu, B.; Chen, Z.; Liu, D.; Li, G.; Liu, H.; He, J.; Wei, L. Discussion on the characteristics and controlling factors of differential enrichment of shale gas in the Wufeng-Longmaxi formations in south China. *Nat. Gas Geosci.* **2020**, *5* (3), 117–128.
- (3) Ma, X. H.; Li, X. Z.; Liang, F.; Wan, Y. J.; Shi, Q.; Wang, Y. H.; Zhang, X. W.; Che, M. G.; Guo, W.; Guo, W. Key control factors of well performance and development strategies optimization in the Weiyuan shale gas play, Sichuan Basin, SW China. *Petrol. Explore. Develop* **2020**, *47* (3), 1–9.
- (4) Ma, X.; Xie, J.; Yong, R.; Zhu, Y.; et al. Geological characteristics and high production control factors of shale gas in Silurian Longmaxi Formation, southern Sichuan Basin, SW China. *Petrol. Explore. Develop* **2020**, *47* (5), 901–915.
- (5) Kuang, L. C.; Dong, D. Z.; He, W. Y.; Wen, S. M.; Sun, S. S.; Li, S. X.; Qiu, Z.; Liao, X. W.; Li, Y.; Wu, J.; et al. Geological characteristics and development potential of transitional shale gas in the east margin of the Ordos Basin, NW China. *Petrol. Explore. Develop* **2020**, *47* (3), 471–482.
- (6) Zhang, M. Q.; Zou, C. N.; Guan, P.; Dong, D. Z.; Sun, S. S.; Shi, Z. S.; Li, Z. X.; Feng, Z. Q.; Li, L. M. Pore-throat characteristics of deep shale gas reservoirs in south of Sichuan Basin: Case study of Longmaxi Formation in Well Z201 of Zigong area. *Nat. Gas Geosci.* **2019**, *30* (9), 1349–1361.
- (7) Zou, C. N.; Zhai, G. M.; Zhang, G. Y.; Wang, H. J.; Zhang, G. S.; Li, J. Z.; Wang, Z. M.; Wen, Z. X.; Li, F.; Liang, Y. B.; et al. Formation, distribution, potential and prediction of global conventional and unconventional hydrocarbon resources. *Petrol. Explore. Develop* **2015**, *42* (1), 14–28.
- (8) Yu, H.; Zhu, Y.; Jin, X.; Liu, H.; Wu, H. Multiscale simulations of shale gas transport in micro/nano-porous shale matrix considering pore structure influence. *J. Nat. Gas Sci. Eng.* **2019**, *64*, 28–40.
- (9) Li, Y.; Kalantari-Dahaghi, A.; Zolfaghari, A.; Dong, P.; Negahban, S.; Zhou, D. Fractal-based real gas flow model in shales: An interplay of nano-pore and nano-fracture networks. *Int. J. Heat Mass Transfer* **2018**, *127*, 1188–1202.
- (10) Dheiaa, A.; Wei, M. Z.; Bai, B. J. Feasibility of CO₂-EOR in Shale-Oil Reservoirs: Numerical Simulation Study and Pilot Tests. *Carbon Management Technol. Conf.*, Houston, Texas, USA, 17–20 July 2017. DOI: [10.7122/485111-MS](https://doi.org/10.7122/485111-MS).
- (11) Ma, X. H.; Xie, J. The progress and prospects of shale gas exploration and exploitation in southern Sichuan Basin, NW China. *Petrol. Explore. Develop* **2018**, *45* (1), 172–182.
- (12) Zhang, L. H.; He, X.; Li, X. G.; Li, K. C.; He, J.; Zhang, Z.; Guo, J. J.; Chen, Y. N.; Liu, W. S. Shale gas exploration and development in the Sichuan Basin: Progress, challenge and countermeasures. *Nat. Gas Ind. B* **2022**, *9* (2), 176–186.
- (13) Shi, X. W.; Wu, W. K.; Zhou, S. W.; Tian, C.; Li, D.; Li, D. Y.; Li, Y.; Cai, C. H.; Chen, Y. L. Adsorption characteristics and

controlling factors of marine deep shale gas in southern Sichuan Basin, China. *J. Nat. Gas Sci. Eng.* **2022**, *7* (2), 61–72.

(14) Gou, Y. Q.; Xu, S.; Hao, F.; Yang, F.; Zhang, B. Q.; Shu, Z. G.; Zhang, A. H.; Wang, Y. X.; Lu, Y. B.; Cheng, X.; et al. Full-scale pores and micro-fractures characterization using FE-SEM, gas adsorption, nano-CT and micro-CT: A case study of the Silurian Longmaxi Formation shale in the Fuling area, Sichuan Basin, China. *Fuel* **2019**, *253*, 167–179.

(15) Yang, Y.-r.; Liu, X.-c.; Zhang, H.; Zhai, G.-y.; Zhang, J.-d.; Hu, Z.-f.; Bao, S.-j.; Zhang, C.; Wang, X.-h.; Yang, X.; Liu, Z.-z.; Xie, T.; Chen, J.; Fang, L.-y.; Qin, L.-j. A review and research on comprehensive characterization of microscopic shale gas reservoir space. *Chi. Geol.* **2019**, *3*, 541–556.

(16) Xu, Z. X.; Guo, S. B. Analysis of the pore structure of shale gas reservoirs based on argon-ion milling SEM and Image. *J. Northeast Pet. Univ.* **2014**, *38* (4), 45–52.

(17) Gao, Z. Y.; Fan, Y. P.; Hu, Q. H.; Jiang, Z. X.; Huang, Z. L.; Wang, Q. Y.; Cheng, Y. Differential development characteristics of organic matter pores and their impact on reservoir space of Longmaxi Formation shale from the South Sichuan Basin. *Pet. Sci. Bull.* **2020**, *5* (1), 1–16.

(18) Chalmers, G. R.; Bustin, R. M.; Power, I. M. Characterization of gas shale pore systems by porosimetry, pycnometry, surface area, and field emission scanning electron microscopy/transmission electron microscopy image analyses: Examples from the Barnett, Woodford, Haynesville, Marcellus, and Doig unit. *AAPG Bull.* **2012**, *96* (6), 1099–1119.

(19) Curtis, M. E.; Ambrose, R. J.; Sondergeld, C. H.; Rai, C. S. Transmission and Scanning Electron Microscopy Investigation of Pore Connectivity of Gas Shales on the Nanoscale. SPE144391, 2011.

(20) Bai, B.; Zhu, R. K.; Wu, S. T.; Cui, J. W.; Su, L.; Li, T. T. New technology and significance of microscopic pore throat structure characterization of unconventional oil and gas tight reservoirs. *Chin. Pet. Explor.* **2014**, *19* (3), 78–86.

(21) Zhang, J.; Sang, S.; Ma, T.; Wang, C. G.; Chen, J. G. Shale Microstructure Extraction Based on Micro-CT and Permeability Inversion. *Geotech Geol Eng.* **2022**, *40*, 3245–3254.

(22) Yang, R.; He, S.; Hu, Q. H.; Hu, D. F.; Zhang, S. W.; Yi, J. Z. Pore characterization and methane sorption capacity of over-mature organic-rich Wufeng and Longmaxi shales in the southeast Sichuan Basin, China. *Mari. Petro. Geol.* **2016**, *77*, 247–261.

(23) Ma, Y.; Zhong, N. N.; Cheng, L. J.; Pan, Z. J.; Li, H. Y.; Xie, Q. M.; Li, C. Pore structure of two organic-rich shales in southeastern Chongqing area: Insight from Focused Ion Beam Scanning Electron Microscope (FIB-SEM). *Petro. Geol. Experi.* **2015**, *47* (1), 109–116.

(24) Xue, H. Q.; Xu, R. N.; Jiang, P. X.; Zhou, S. W. Characterization of rock microstructure using 3D X-ray computed tomography. *Chin. J. Theor. Appl. Mech.* **2015**, *47* (6), 1073–1078.

(25) Liu, X. F.; Song, D. z.; He, X. Q.; Wang, Z. P.; Zeng, M. R.; Deng, K. Nanopore structure of deep-burial coals explored by AFM. *Fuel* **2019**, *246*, 9–17.

(26) Xu, H.; Zhou, W.; Zhang, R.; Liu, S. M.; Zhou, Q. M. Characterizations of pore, mineral and petrographic properties of marine shale using multiple techniques and their implications on gas storage capability for Sichuan Longmaxi gas shale field in China. *Fuel* **2019**, *241*, 360–371.

(27) Yang, F.; Ning, Z. F.; Wang, Q.; Zhang, R.; Krooss, B. M. Pore structure characteristics of lower Silurian shales in the southern Sichuan Basin, China: Insights to pore development and gas storage mechanism. *Int. J. Coal Geol.* **2016**, *156*, 12–24.

(28) Chen, Y.; Wei, L.; Mastalerz, M.; Schimmelmann, A. The effect of analytical particle size on gas adsorption porosimetry of shale. *Int. J. Coal Geol.* **2015**, *138*, 103–112.

(29) Gai, S. H.; Liu, Q. H.; He, S. L.; Mo, S. Y.; Chen, S.; Liu, R. H.; Huang, X.; Tian, J.; Lv, X. C.; Wu, D. X.; et al. Shale reservoir characteristics and exploration potential in the target: A case study in the Longmaxi Formation from the southern Sichuan Basin of China. *J. Nat. Gas Sci. Eng.* **2016**, *31*, 86–97.

(30) Sang, Q. Experimental method and effective production conditions of shale oil and gas seepage. *Doctoral thesis of China University of Petroleum*, 2017, Qingdao, Shandong.

(31) Wang, Y. M.; Wang, H. K.; Zhang, C. C.; Li, X. J.; Dong, D. Z. Fracture pore evaluation of the Upper Ordovician Wufeng to Lower Silurian Longmaxi Formations in southern Sichuan Basin, SW China. *Petro. Explor. Develop* **2017**, *44* (4), 563–572.

(32) Liu, Y. W.; Gao, D. P.; Li, Q.; Wan, Y. Z.; Duan, W. J.; Zeng, X. G.; Li, M. Y.; Su, Y. W.; Fan, Y. B.; Li, S. H. Several frontier issues in mechanics of shale gas exploitation. *Adv. Mech* **2019**, *49* (1), 201901.

(33) Liu, Y.; Yao, B.; Liu, D. M.; Zheng, S. J.; Sun, G. X.; Chang, Y. H. Shale pore size classification: An NMR fluid typing method. *Mari. Petro. Geol.* **2018**, *96*, 591–601.

(34) Zhang, P. F.; Lu, S. F.; Li, J. Q.; Chen, C.; Xue, H. T.; Zhang, J. Petrophysical characterization of oil-bearing shales by low-field nuclear magnetic resonance (NMR). *Mari. Petro. Geol.* **2018**, *89*, 775–785.

(35) Li, J.; Jin, W. J.; Wangang, L.; Wu, Q.; Lu, J.; Hao, S. Quantitative evaluation of organic and inorganic pore size distribution by NMR: A case from the Silurian Longmaxi Formation gas shale in Fuling area, Sichuan Basin. *Oil Gas Geol.* **2016**, *37* (1), 129–134.

(36) Ning, Z. F.; Wang, B.; Yang, F.; Zeng, Y.; Chen, J. E.; Zhang, L. Micro-scale effects of micro-seepage in shale reservoirs. *Petro. Explor. Develop* **2014**, *41* (4), 492–499.

(37) Lin, M.; Jiang, W. B.; Li, Y.; Zhang, R. B. Some problems in shale oil (gas) micro-scale flow. *Bull. Miner. Petro. Geochem.* **2015**, *34* (1), 18–28.

(38) Luo, Z. F. C.; Zhang, N. L.; Zhao, L. Q.; Yao, L. M.; Liu, F. Seepage-stress coupling mechanism for intersections between hydraulic fractures and natural fractures. *J. Pet. Sci. Eng.* **2018**, *171*, 37–47.

(39) Raoof, A.; Hassanizadeh, S. M. A New Method for Generating Pore-Network Models of Porous Media. *Transp Porous Med.* **2010**, *81*, 391–407.

(40) Yao, J.; Song, W. H.; Wang, D. Y.; Sun, H.; Li, Y. Multi-scale pore network modelling of fluid mass transfer in nano-micro porous media. *Int. J. Heat Mass Transfer* **2019**, *141*, 156–167.

(41) Yao, J.; Zhao, J. L.; Zhang, M.; et al. Microscale shale gas flow simulation based on Lattice Boltzmann method. *Acta Pet. Sin.* **2015**, *36* (10), 1280–1289.

(42) Wang, S.; Feng, Q. H.; Cha, M. Molecular dynamics simulation of the occurrence of liquid alkanes in shale organic matter pores and fractures. *Petro. Explor. Dev.* **2015**, *42* (6), 772–778.

(43) Li, Y. X.; Hu, Z. M.; Liu, X. G.; Duan, X. G.; Gao, S. S.; Wang, W. D.; Chang, J. Pressure-dependent Equilibrium Molecular Simulation of Shale Gas and Its Distribution and Motion Characteristics in Organic-rich Nano-slit. *Fuel* **2019**, *237*, 1040–1049.

(44) Li, Y.; Hu, Z.; Duan, X.; Wang, X.; Shi, J.; Zhan, H. The general form of transport diffusivity of shale gas in organic-rich nano-slits — a molecular simulation study using Darken approximation. *Fuel* **2019**, *249*, 457–471.

(45) Li, Y. X.; Hu, Z. M.; Liu, X. G.; Gao, S. S.; Duan, X. G.; Chang, J.; Wu, J. F. Insights into interactions and microscopic behavior of shale gas in orgasimulation[J]. *J. Nat. Gas Sci. Eng.* **2018**, *59*, 309–325.

(46) Song, W. H.; Yao, J.; Li, Y.; Sun, H.; Zhang, L.; Yang, Y. F.; Zhao, J. L.; Sui, H. G. Apparent gas permeability in an organic-rich shale reservoir [J]. *Fuel* **2016**, *181*, 973–984.

(47) Liu, P.; Harder, E.; Berne, B. J. On the calculation of diffusion coefficients in confined fluids and interfaces with an application to the liquid–vapor interface of water[J]. *J. Phys. Chem. B* **2004**, *108* (21), 6595–6602.

(48) Mosher, K.; He, J.; Liu, Y.; Rupp, E.; Wilcox, J. Molecular simulation of methane adsorption in micro-and mesoporous carbons with applications to coal and gas shale systems. *Int. J. Coal Geol.* **2013**, *109*, 36–44.

(49) Skoulidas, A. I.; Ackerman, D. M.; Johnson, J. K.; Sholl, D. S. Rapid transport of gases in carbon nanotubes[J]. *Phys. Rev. Lett.* **2002**, *89* (18), 185901.

- (50) Song, X.; Chen, J. K. A comparative study on poiseuille flow of simple fluids through cylindrical and slit-like nanochannels[J]. *Int. J. Heat Mass Transfer* **2008**, *51* (7–8), 1770–1779.
- (51) Zuo, L.; Xiong, W.; Guo, W.; Gao, S. S.; Hu, Z. M. The Mechanism of Occurrence State of Shale Gas. *Xinjiang Petro. Geol.* **2014**, *35* (2), 158–162.
- (52) He, Z. L.; Nie, H. K.; Hu, D. F.; Jiang, T. X.; Wang, R. Y.; Zhang, Y. Y.; Zhang, G. R.; Liu, Z. Y. Geological problems in the effective development of deep shale gas: a case study of Upper Ordovician Wufeng-Lower Silurian Longmaxi formations in Sichuan Basin and its periphery. *Acta Pet. Sin.* **2020**, *41* (4), 379–391.
- (53) Chang, J.; Gao, S. S.; Hu, Z. M.; Xue, H. Flow mechanism of high-pressure gas microtubes. *Acta Pet. Sin.* **2015**, *36* (12), 1559–1563.
- (54) Hu, Z. M.; Duan, X. G.; Chang, J.; Li, W. G.; Shen, R. Simulation experiments on the development characteristics of shale gas and coalbed methane. *Special Oil and Gas Reservoirs* **2019**, *26* (4), 125–130.
- (55) Singh, H.; Javadpour, F.; Etehadtavakkol, A.; Darabi, H. Nonempirical Apparent Permeability of Shale. *SPE Res. Eval & Eng.* **2014**, *17* (03), 414–424.
- (56) Jones, F. O.; Owens, W. W. A Laboratory study of low-permeability gas sands. *J. Petro. Technol.* **1980**, *32* (9), 1631–1640.
- (57) Florence, F. A.; Rushing, J. A.; Nwesham, K. E.; Blasingame, T. A. Improved permeability prediction relations for low permeability sands. *SPE Rocky Mountain Oil & Gas Tech. Sympos.*, Denver, Colorado, SPE 107954, 2007: 1–15.
- (58) Ertekin, T.; King, G. R.; Schwerer, F. C. Dynamic gas slippage: A unique dual-Mechanism approach to the flow of gas in tight formations [J]. *SPE Form Eval.* **1986**, *1* (1), 43–52.
- (59) Michel, G. G.; Sigal, R. F.; Civan, F.; Devegowda, D. Parametric investigation of shale gas production considering nano-scale pore size distribution, formation factor, and non-Darcy flow mechanisms. *Paper SPE-147438-MS presented at the SPE Annu. Tech. Conf. Exhib.*, 30 October–2 November 2011, Denver, Colorado. DOI: 10.2118/147438-MS.
- (60) Sakhaee-Pour, A.; Bryant, S. L. Gas Permeability of Shale. *SPE Res. Engg. and Eval* **2012**, *15* (4), 401–409.
- (61) Civan, F.; Rai, C. S. S.; Sondergeld, C. H. H. Determining Shale Permeability to Gas by Simultaneous Analysis of Various Pressure Tests. *SPE J.* **2012**, *17* (6), 717–726.
- (62) Beskok, A.; Karniadakis, G.-E. A Model for flows in channels, pipes, and ducts at micro and nano scales. *Microscale Thermophys. Eng.* **1999**, *3* (1), 43–77.
- (63) Singh, H.; Javadpour, F. Langmuir Slip-Langmuir sorption permeability model of shale. *Fuel* **2016**, *164* (1), 28–37.
- (64) Javadpour, F.; Fisher, D.; Unsworth, M. Nanoscale Gas Flow in Shale Gas Sediments. *J. Can. Petro Technol.* **2007**, *46* (10), 55–61.
- (65) Javadpour, F. Nanopores and Apparent Permeability of Gas Flow in Mudrocks (Shales and Siltstone). *Petro. Soc. Can.* **2009**, *48* (8), 16–21.
- (66) Duan, X.; Hu, Z.; Shao, N.; Li, W.; Li, Y.; Chang, J.; Shen, R. Establishment of a new slip permeability model of gas flow in shale nanopores based on experimental and molecular dynamics simulations studies. *J. Pet. Sci. Eng.* **2020**, *193*, 107365.
- (67) Li, Y.; Liu, X.; Hu, Z.; Gao, S. S.; Duan, X. G.; Chang, J. A new method for the transport mechanism coupling of shale gas slippage and diffusion. *Acta Phys. Sin.* **2017**, *66* (11), 1000–3290.
- (68) Li, Y. X.; Liu, X. G.; Gao, S. S.; Duan, X. G.; Hu, Z. M.; Chen, X. K.; Shen, R.; Guo, H. K.; An, W. G. A generalized model for gas flow prediction in shale matrix with deduced coupling coefficients and its macroscopic form based on real shale pore size distribution experiments. *J. Pet. Sci. Eng.* **2020**, *187*, 106712.
- (69) Loucks, R. G.; Reed, R. M.; Ruppel, S. C.; Jarvie, D. M. Morphology, genesis, and distribution of nanometer-scale pores in siliceous mudstones of the Mississippian Barnett Shale. *J. Sediment. Res.* **2009**, *79* (12), 848–861.
- (70) Sladek, K. J.; Gilliland, E. R.; Baddour, R. F. Diffusion on surfaces. II. Correlation of diffusivities of physically and chemically adsorbed species. *Ind. Eng. Chem. Fundam.* **1974**, *13* (2), 100–105.
- (71) Wu, K. L.; Chen, Z. X.; Li, X. F.; Xu, J. Z.; Li, J.; Wang, K.; Wang, H.; Wang, S. H.; Dong, X. H. Flow behavior of gas confined in nanoporous shale at high pressure: Real gas effect. *Fuel* **2017**, *205*, 173–183.
- (72) Niu, C.; Hao, Y.; Li, D.; Lu, D. Second-order gas-permeability correlation of shale during slip flow. *SPE J.* **2014**, *19* (5), 786–792.
- (73) Chen, J.; Yu, H.; Fan, J. C.; Wang, F. C.; Lu, D. T.; Liu, H.; Wu, H. G. Channel-width dependent pressure-driven flow characteristics of shale gas in nanopores. *AIP Adv.* **2017**, *7* (4), 045217.
- (74) Michel, G. G.; Sigal, R. F.; Civan, F.; Devegowda, D. Parametric investigation of shale gas production considering nano-scale pore size distribution, formation factor, and non-Darcy flow mechanisms. *Paper SPE-147438-MS presented at the SPE Annu. Tech. Conf. Exhib.*, 30 October–2 November 2011, Denver, Colorado. DOI: 10.2118/147438-MS.
- (75) Xiong, X.; Devegowda, D.; Michel, G. G.; Sigal, R. F.; Civan, F. A fully-coupled free and adsorptive phase transport model for shale gas reservoirs including non-Darcy flow effects. *Paper SPE-159758-MS presented at the SPE Annu. Tech. Conf. Exhib.*, 8–10 October 2012, San Antonio, Texas. DOI: 10.2118/159758-MS.
- (76) Yang, F.; Zheng, H.; Lyu, B.; Wang, F.; Guo, Q.; Xu, H. Experimental Investigation about Gas Transport in Tight Shales: An Improved Relationship between Gas Slippage and Petrophysical Properties[J]. *Energy Fuels* **2021**, *35* (5), 3937–3950.
- (77) Cao, P. X.; Liu, J. S.; Leong, Y. K. Combined impact of flow regimes and effective stress on the evolution of shale apparent permeability [J]. *J. Unconv. Oil Gas Resour.* **2016**, *14*, 32–43.
- (78) Guo, W.; Hu, Z. M.; Zuo, L.; Gao, S. S.; Yu, R. Z.; Zeng, B. Shale matrix desorption-diffusion-seepage coupling experiment and mathematical mode. *Chin. J. Theor. Appl. Mech.*, **2015**, *47* (6), 916–922.
- (79) Wang, S. Q. Shale gas exploitation: Status, issues and prospects. *Nat. Gas Ind. B* **2018**, *5* (1), 60–74.
- (80) Duan, X. G.; Hu, Z. M.; Gao, S. S.; Shen, R.; Liu, H. X.; Chang, J.; Wang, L. Shale high pressure isothermal adsorption curve and production dynamic experiments of gas well. *Petrol. Explore. Develop* **2018**, *45* (1), 127–135.
- (81) Gao, S. S.; Liu, H. X.; Ye, L. Y.; Hu, Z. M.; An, W. G. Physical simulation experiment and numerical inversion of the full life cycle of shale gas well. *Acta Pet. Sin.* **2019**, *4* (2), 181–190.
- (82) Li, W. B.; Lu, S. F.; Li, J. Q.; Wei, Y. B.; Zhao, S. X.; Zhang, P. F.; Wang, Z. Y.; Li, X.; Wang, J. Research progress on isotopic fractionation in the process of shale gas/coalbed methane migration [J]. *Petrol. Explore. Develop* **2022**, *49* (5), 1069–1084.
- (83) Gao, S. S.; Liu, H. X.; Ye, L. Y.; Hu, Z. M.; An, W. G. Full life cycle physical simulation experiment and numerical inversion of shale gas well. *Acta Pet. Sin.* **2018**, *39* (4), 435–444.
- (84) Gao, S. S.; Liu, H. X.; Ye, L. Y.; Hu, Z. M.; Chang, J.; An, W. G. Coupling model of gas diffusion and seepage in SRV region of shale gas reservoir. *Nat. Gas Ind. B* **2017**, *4* (2), 120–126.
- (85) Roy, S.; Raju, R.; Chuang, H. F.; Cruden, B. A.; Meyyappan, M. Modeling gas flow through microchannels and nanopores. *J. Appl. Phys.* **2003**, *93* (8), 4870–4879.
- (86) Kazemi, M.; Takbiri-Borujeni, A. An analytical model for shale gas permeability. *Int. J. Coal Geol* **2015**, *146*, 188–197.
- (87) Baihy, J. D.; Altman, R. M.; Malpani, R.; Malpani, R.; Luo, F. Shale gas production decline trend comparison over time and basins. *SPE Annu. Tech. Conf. Exhib.*, 19–22 September 2010, Florence, Italy. DOI: 10.2118/135555-MS.
- (88) Shen, W. J.; Zheng, L. G.; Oldenberg, C. M.; Oldenburg, C. M.; Cihan, A.; Wan, J. M.; Tokunaga, T. K. Methane Adsorption and Diffusion in Shale Rocks-A Numerical Study Using the Dusty Gas Model in Tough2/EOS7C-ECBM. *Transp. Porous Media* **2018**, *123* (3), 521–531.
- (89) Ma, X. H.; Shen, W. J.; Li, X. Z.; Hu, Y.; Liu, X. H.; Lu, X. B. Experimental investigation on water adsorption and desorption

isotherms of the longmaxi shale in the Sichuan basin, China. *Sci. Rep.* **2020**, *10*, 13434.

(90) Hu, Z. M.; Duan, X. G.; He, Y. B.; Wu, J. F.; Chang, J.; Liu, L.; Wu, K.; Ma, Z. Y. The influence of reservoir connate water on the occurrence and flow ability of shale gas. *Nat. Gas Ind. B* **2018**, *38* (7), 45–52.

(91) Shen, R.; Hu, Z. M.; Guo, H. K.; Jiang, B. C.; Miao, S.; Li, W. G. Occurrence space and gas-bearing regularity of Longmaxi Formation shale in Changning, Sichuan Basin. *Lithol. Reservoirs* **2018**, *30* (3), 1–11.

(92) Bello, R. O.; Wattenbarger, R. A. Modelling and analysis of shale gas production with a skin effect. *J. Can. Pet. Tech* **2010**, *49*, 37–48.

(93) Ahmadi, H. A.; Almarzooq, A.; Wattenbarger, R. Application of linear flow analysis to shale gas wells-field cases. In *SPE Unconv. Gas Confer.*, Pittsburgh, 2010.

(94) Brown, M.; Ozkan, E.; Raghavan, R.; Kazemi, H. Practical solutions for pressure-transient responses of fractured horizontal wells in unconventional shale reservoirs. *SPE Reservoir Evaluation Eng.* **2011**, *14*, 663–676.

(95) Stalgorova, K.; Mattar, L. Analytical model for unconventional multifractured composite systems. *SPE Reservoir Evaluation Eng.* **2013**, *16*, 246–256.

(96) Zhu, W. Y.; Ma, D. X.; Qi, Q.; Song, Z. Y.; Yue, M. Multi-zone coupling productivity analysis of horizontal wells with complex fractured web rock. *Nat. Gas Ind. B* **2017**, *037* (007), 60–68.

(97) Duan, Y. G.; Wei, M. Q.; Li, J. Q.; Tang, Y. Shale gas seepage mechanism and fractured well' production evaluation. *J. Chongqing Univ.* **2011**, *34* (04), 62–66.

(98) Li, Y. L.; Liu, X. G.; Hu, Z. M.; Duan, X. G.; Chang, J.; Zhou, G. Z. Research progress in fracture network simulation of shale reservoirs. *Petro. Geophys. Pros.* **2019**, *54* (2), 480–493.

(99) Wang, L.; Hu, Z. M.; Xiong, W.; Gao, S. S.; Duan, X. G.; Chen, X. K. Physical simulation of shale matrix supply capacity and gas production law. *Daqing Petro. Geol. Develop.* **2018**, *37* (5), 14–146.

(100) Zuo, L.; Hu, Z. M.; Cui, Y. X.; Xiong, W.; Gao, S. S.; Shen, R.; Xiao, H. R. Experimental study on shale adsorption kinetics at high temperature and pressure. *J. Chin. Coal Soc.* **2016**, *41* (8), 2017–2023.

(101) Duan, X. G.; An, W. G.; Hu, Z. M.; Gao, S. S.; Ye, L. Y.; An, W. G. Experimental study on stress sensitivity of shale fractures in the Silurian Longmaxi Formation in the Sichuan Basin. *Nat. Gas Geosci.* **2017**, *28* (9), 1416–1424.

(102) Ma, Y.; Zhong, N. N.; Cheng, L. J.; Pan, Z. J.; Li, H. Y.; Xie, Q. M.; Li, C. Pore structure of two organic-rich shales in southeastern Chongqing area: Insight from Focused Ion Beam Scanning Electron Microscope (FIB-SEM) [J]. *Pet. Geol. Exp.* **2015**, *47* (1), 109–116.